Letter

Quantum paraelectricity and structural phase transitions in strontium titanate beyond density functional theory

Carla Verdi,[1,*] Luigi Ranalli,[1] Cesare Franchini,[1,2] and Georg Kresse[1,3]
[1]*University of Vienna, Faculty of Physics, Computational Materials Physics, Kolingasse 14-16, 1090 Vienna, Austria*
[2]*Department of Physics and Astronomy, Alma Mater Studiorum - Università di Bologna, Bologna, Italy*
[3]*VASP Software GmbH, Sensengasse 8, 1090 Vienna, Austria*

(Received 22 November 2022; accepted 21 February 2023; published 16 March 2023)

We demonstrate an approach for calculating temperature-dependent quantum and anharmonic effects with beyond density-functional theory accuracy. By combining machine-learned potentials and the stochastic self-consistent harmonic approximation, we investigate the cubic to tetragonal transition in strontium titanate and show that the paraelectric phase is stabilized by anharmonic quantum fluctuations. We find that a quantitative understanding of the quantum paraelectric behavior requires a higher-level treatment of electronic correlation effects via the random phase approximation. This approach enables detailed studies of emergent properties in strongly anharmonic materials beyond density-functional theory.

DOI: 10.1103/PhysRevMaterials.7.L030801

Perovskite oxides are one of the most versatile classes of materials, displaying a huge array of properties such as piezoelectricity, ferromagnetism, ferroelectricity, and multiferroicity, as well as metal-insulator transitions and superconductivity. These fascinating properties are linked to several technological applications, ranging from superconductors to catalysis, thermoelectric processes, and nanoelectronics [1–7]. A key role is played by structural instabilities that may distort the ideal cubic perovskite structure, resulting in a rich structural phase diagram and property landscape. Crucially, structural instabilities are also found to compete with ferroelectricity and may thus suppress the latter [8,9]. These phenomena are governed by lattice quantum anharmonicity, that is, the presence of higher-order interactions on top of the harmonic vibrations of the crystal.

Strontium titanate ($SrTiO_3$) is a paradigmatic example of a perovskite oxide with strongly anharmonic lattice dynamics and is a ubiquitous playground for emergent phenomena in complex oxides and heterostructures such as two-dimensional (2D) electron gases, polaronic properties, and dilute superconductivity [1,10–13]. It famously undergoes an antiferrodistortive (AFD) transition from a cubic to a tetragonal structure below 105 K [14], with high proximity to ferroelectricity. In $SrTiO_3$, ferroelectricity is only incipient, meaning that the structure is found to remain paraelectric down to zero kelvin, which is attributed to quantum fluctuations [15]. Yet, this effect can easily be overcome by small perturbations such as strain or isotope substitution [16,17]. The importance of quantum paraelectricity and its tunability has been recognized in relation to the exotic superconducting and transport behavior of $SrTiO_3$ at low carrier doping [18–20], with the ferroelectric (FE) soft mode fluctuations likely playing a key role in providing the pairing mechanism for superconductivity in the quantum critical regime [21,22]. A detailed quantitative understanding of the ground-state properties of quantum paraelectric materials such as $SrTiO_3$, as well as their temperature dependence, thus underpins both the study of exotic physics and the advancement of technological applications [23,24].

First-principles methods based on density-functional theory (DFT) have been extensively employed to investigate the strength of the AFD and FE instabilities in $SrTiO_3$ and the influence of strain or doping at 0 K and within the harmonic approximation [25–27]. An accurate microscopic description of temperature-dependent anharmonic processes beyond simple approximations, however, poses severe challenges. While some approaches exist [28–33], they are either prohibitively expensive beyond simple materials or lack a general and consistent procedure to capture all quantum and anharmonic effects to high orders. For these reasons, atomistic studies of quantum fluctuations are generally limited to path-integral Monte Carlo calculations using *ad hoc* parametrized effective Hamiltonians [34,35] or to solving a one-dimensional (1D) or 2D lattice-nuclear Schrödinger equation from first principles, thereby neglecting intermode phonon couplings and structural changes for all internal and lattice degrees of freedom [36,37]. Finally, it is still unknown how accurately DFT can describe these subtle anharmonic processes, which are strongly functional dependent [26,36,38].

In this Letter, we propose a general framework to investigate the anharmonic properties of this class of materials and their temperature dependence with beyond-DFT accuracy, and we demonstrate it for $SrTiO_3$. We employ the stochastic self-consistent harmonic approximation (SSCHA) [39] in combination with machine-learned interatomic potentials or force fields (MLFFs) [40]. We show that this method seamlessly enables us to fully capture strong anharmonicities while

*Present address: School of Physics, The University of Sydney, New South Wales, 2006, Australia; carla.verdi@univie.ac.at

retaining first-principles accuracy, and further unlocks the possibility to perform many-body calculations beyond DFT. Here we train an MLFF based on the random-phase approximation (RPA) [41] following the principles of Δ-machine learning [42]. We analyze the effects of anharmonicity in renormalizing the phonon frequencies, lattice parameters and internal degrees of freedom, and we characterize the displacive transition between the cubic and tetragonal phase driven by the collapse of the zone-boundary AFD instability. All employed exchange-correlation functionals find that the paraelectric phase is stabilized at 0 K by anharmonic quantum fluctuations, but only the RPA delivers accurate quantitative agreement with experimental data.

We start by outlining our strategy for computing anharmonic properties. We use the SSCHA method [30,39], a stochastic approach to the self-consistent harmonic approximation [43,44], which allows us to treat anharmonicity at a nonperturbative level, including nuclear quantum effects. Through a stochastic minimization of the free energy functional, the SSCHA yields a variational approximation for the quantum anharmonic ground state of the system. This method delivers highly accurate data [30,45,46], but its applicability to large systems is limited by the need for computing *ab initio* energies and forces for several thousand supercells [see the Supplemental Material (SM) [47] for additional information]. A natural strategy to reduce this computational cost is turning to surrogate models to compute the potential energy surface and its derivatives. The ideal solution is offered by machine-learned potentials. MLFFs provide fully flexible models allowing to simultaneously predict the energies, atomic forces and stress tensor components of a given system orders of magnitude faster than a standard *ab initio* calculation, albeit retaining almost the same level of accuracy [40,56]. Notably, they can accurately capture the harmonic lattice dynamics as well as the anharmonic higher-order contributions, including the coupling of phonons and lattice distortions, without the need of *ad hoc* parametrizations [57,58]. They are capable of describing different structural phases at the same time over a wide range of temperatures, and are not overly sensitive to the training data set. In contrast, empirical interatomic potentials, effective Hamiltonians, or so-called second-principles parametrizations are not able to simultaneously satisfy all these demands [59–61]. The combined SSCHA-MLFF approach outlined is orders of magnitude faster than path-integral based methods, especially in the low-temperature regime, and has the advantage that anharmonic phonon frequencies are easily obtained.

To start, we train a kernel-based MLFF for $SrTiO_3$ from a database of DFT calculations adopting the PBEsol functional [62], using the VASP package [63–65]. The MLFF is trained on the fly during molecular dynamics simulations, where the selection of new structures is controlled by Bayesian error estimation [65]. More details are given in the SM [47]. The training data set consists of 626 structures of 320 atoms each, sampling the configurational phase space of $SrTiO_3$ up to 350 K. The root-mean-square errors in the energies, forces, and stress tensors predicted by the MLFF for a test data set are 0.18 meV/atom, 0.037 eV/Å, and 0.32 kbar, respectively [47]. We highlight that attaining such small errors is crucial in the present paper, where energy differences of less than 1 meV/atom due to the interplay of different instabilities ought to be captured, as will be shown in the following.

We first investigate the FE instability by looking at the 1D potential energy surface obtained by displacing the atoms in the unit cell along the FE soft modes driving the instability, as shown in Figs. 1(a) and 1(b). In the tetragonal structure (illustrated in SM Fig. S1 [47]), the FE instability is split into a mode polarized parallel to the tetragonal axis c, A_{2u} [Fig. 1(a)] and a doubly degenerate one perpendicular to it, E_u [Fig. 1(b)]. Both modes are imaginary in standard harmonic calculations, as reflected by the double-well shape of the energy curves. The well depth of E_u is larger than A_{2u}, however, in both cases it is very shallow (less than 0.5 meV per formula unit, f.u.), suggesting that quantum fluctuations can easily overcome the energy barrier. Note that our MLFF reproduces precisely this instability. We then perform calculations using the rSCAN meta-GGA functional [66] as well as the HSE06 hybrid functional [67,68]. As seen in Figs. 1(a) and 1(b), rSCAN slightly increases the barriers to around 0.5 meV/f.u., and HSE06 yields even stronger FE instabilities. Similar calculations performed on two other systems, the quantum paraelectric $KTaO_3$ and the ferroelectric $BaTiO_3$, also show a marked dependence of the FE instability on the chosen density functional [Figs. 1(g) and 1(h)].

To cure this strong functional dependence, we seek to go beyond semilocal and hybrid DFT by adopting the accurate, but computationally costly, many-body RPA method [41,69]. RPA total energy calculations are at least two orders of magnitude more expensive than standard DFT ones, or three when forces are also computed [70]. To accelerate RPA calculations via machine learning, we train an RPA-based MLFF using the principles of Δ-learning [42,71]. As described in the SM [47] in more detail, we compute the RPA corrections to the DFT energies and forces for a reduced set of structures. By training an MLFF that accurately reproduces these corrections, we can predict RPA-level energies and forces for any given structure. Incidentally, we use a similar procedure to also obtain an MLFF that reproduces the rSCAN potential energy surface. This yields low RMSEs comparable to the ones obtained for PBEsol, and excellent predictions for the phonon frequencies and the potential energy surfaces of the FE modes [47]. The latter are shown in Figs. 1(a) and 1(b). We see that the RPA has a dramatic effect on the FE instability, making the energy barrier as high as almost 7 meV/f.u. Also in the case of $KTaO_3$ [Fig. 1(g)] and $BaTiO_3$ [Fig. 1(h)] the RPA increases the energy barrier, though for $BaTiO_3$ the well depth is largest using HSE06.

To gain more insight into the strength of the FE instability as described by different approximations to the exchange and correlation, we consider its behavior as a function of volume size and shape in $SrTiO_3$. To illustrate this, we compute a 2D energy map by displacing the atoms from their optimized tetragonal positions along the FE modes and varying the values of the tetragonal distortion c/a. Figures 1(c) and 1(d) show the results obtained for the A_{2u} and E_u modes, respectively, at the equilibrium volume using our RPA-based MLFF, while in Fig. 1(f) a volume 0.75% smaller than the equilibrium one is used for the E_u mode. After inspecting these plots, we can conclude that (i) both the E_u and A_{2u} instabilities display a strong dependence on strain but they behave in opposite

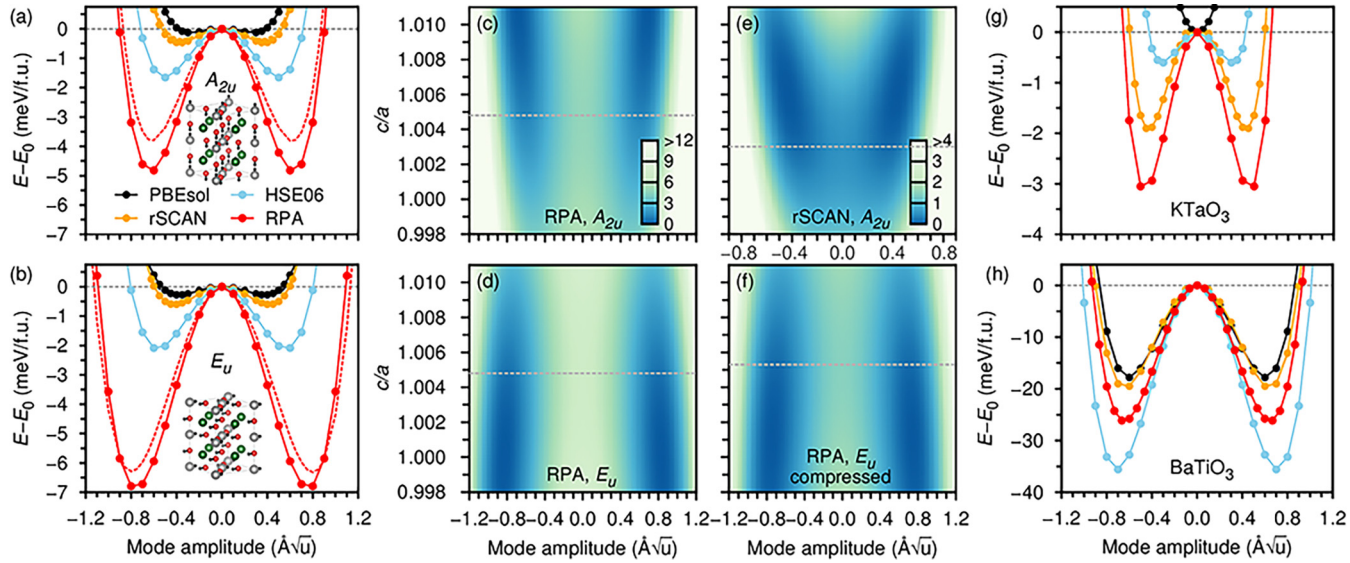

FIG. 1. Ferroelectric potential energy surfaces (PES). (a), (b) 1D PES of the A_{2u} and E_u FE soft modes in tetragonal $SrTiO_3$, respectively, depicted in the insets. Results obtained using the PBEsol, rSCAN and HSE06 functionals are shown, as well as the RPA. The dashed lines are for the MLFFs trained on PBEsol, rSCAN (not visible) and the RPA. (c), (d) Corresponding 2D PES calculated at the equilibrium volume using the RPA-based MLFF as a function of FE mode amplitude and c/a ratio. (e) 2D PES for atomic displacements along the A_{2u} mode using rSCAN. (f) 2D PES for the E_u mode calculated from the RPA, after compressing the volume by 0.75%. The color maps indicate energies in meV/f.u, and the color map in (c) is for all the RPA-based calculations [(c), (d), and (f)]. The horizontal lines mark the equilibrium c/a values. (g),(h) 1D ferroelectric PES calculated for (g) $KTaO_3$ and (h) $BaTiO_3$ in the cubic phase. In (g), the orange points are obtained using SCAN.

ways as a function of the lattice elongation. The A_{2u} instability becomes stronger with increasing c/a values and the E_u one gets weaker, while they both decrease as a function of volume (consistent results are obtained for volume expansion, see SM Figs. S6 and S7 [47]). Moreover, (ii) the RPA description of the electronic structure generally yields much stronger FE instabilities than rSCAN [Fig. 1(e)] and PBEsol (SM Fig. S5 [47]), even when considering the effects of strain. These observations have important implications when considering anharmonic fluctuations and the coupling with lattice distortions, as we will see in the following.

We now proceed to include anharmonicity by combining SSCHA and MLFFs. Figure 2 displays the anharmonic

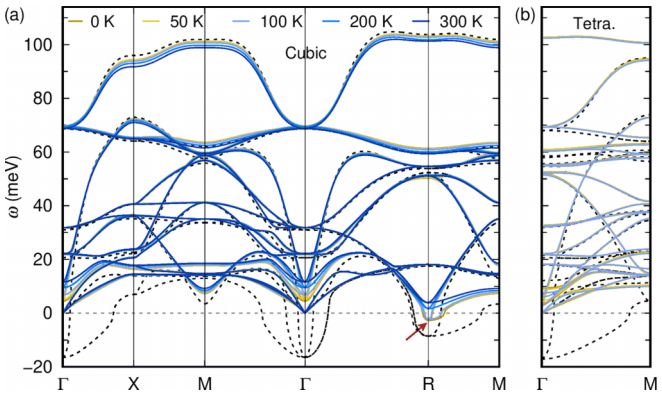

FIG. 2. Temperature-dependent phonon dispersions of (a) cubic and (b) tetragonal $SrTiO_3$ calculated using the SSCHA and the MLFF trained on the RPA. The dashed lines are the harmonic results, and negative values denote imaginary frequencies.

phonon dispersions of tetragonal and cubic $SrTiO_3$ at different temperatures, computed at the RPA level from the free-energy Hessian [39,47]. Here, for each temperature we adopt the experimental lattice volume, and we allow the c/a ratio to relax so as to minimize the temperature-dependent anharmonic free energy. The corresponding harmonic dispersions are also shown. As expected, in the harmonic approximation the cubic structure exhibits unstable phonon modes with imaginary frequencies at the Γ and R points. The latter is responsible for the low-temperature AFD transformation into the tetragonal structure and indeed remains unstable below the transition temperature even when anharmonic effects are included [see the arrow in Fig. 2(a)]. In the tetragonal structure, this triply degenerate mode becomes a zone-center phonon and splits into an A_{1g} mode, corresponding to oxygen rotations around the c axis, and a doubly degenerate E_g mode, both found to be stable. On the contrary, in both structures the FE modes at Γ are stable at every temperature when quantum anharmonic fluctuations are accounted for. This confirms the quantum paraelectric ground state of $SrTiO_3$. Similar conclusions apply for PBEsol and rSCAN, as reported in SM Fig. S9 [47].

Both the AFD and FE modes show a marked temperature dependence. As can be seen in Fig. 3(a), the anharmonic phonon frequency of the AFD mode in the high-temperature cubic phase shows the softening characteristic of displacive phase transitions. The large splitting of the A_{1g} and E_g modes below the transition temperature T_c is in line with the measured data [14,72], with the A_{1g} mode higher in energy than the E_g one. A square-root Curie-Weiss fit yields values of T_c of 214 K for PBEsol calculations, 96 K for rSCAN, and 172 K for the RPA. In Fig. 3(c), the RPA free energy difference between the cubic and tetragonal phase is shown, as well as

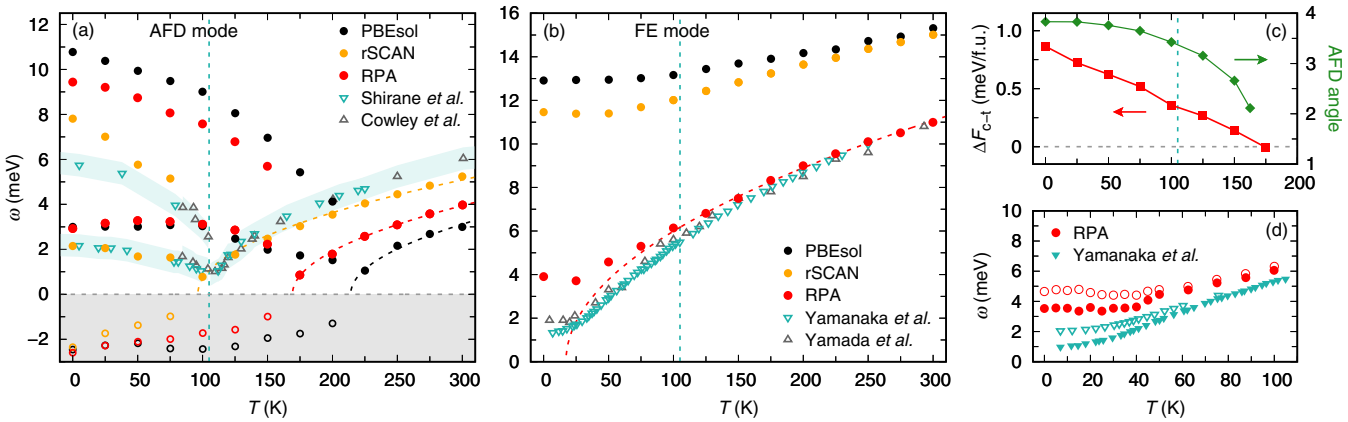

FIG. 3. AFD phase transition and quantum paraelectricity in $SrTiO_3$. (a) Temperature dependence of the AFD mode calculated using MLFFs trained on PBEsol (black), rSCAN (orange) and the RPA (red). The empty symbols in the negative frequency region represent imaginary phonons obtained when the symmetry of the structure is kept cubic at each temperature, and the shaded regions are a guide to the eye. (b) Temperature dependence of the FE mode calculated using the same MLFFs. When the structure is tetragonal, averages over the A_{2u} and E_u modes are shown. In (a) and (b), experimental measurements from Refs. [14,72–74] are also reported. The dashed vertical lines indicate the experimental AFD transition temperature, and the dashed curves are Curie-Weiss fits. (c) Free-energy difference between the cubic and tetragonal structures and AFD rotation angle in the tetragonal phase as a function of temperature obtained from the RPA. Above 175 K, the most stable structure is the cubic one. (d) Close-up of the FE soft mode in the low-temperature region from the RPA and hyper-Raman spectroscopy [73], showing the splitting into the A_{2u} (empty symbols) and E_u (filled symbols) branches.

the AFD rotation angle, in line with the predicted T_c from the phonon collapse. While none of the methods accurately reproduces the experimental T_c of 105 K, rSCAN is in fairly good agreement. We find that this result is linked to the superior performance of rSCAN in describing the equilibrium tetragonal structure, in particular the AFD rotation angle and c/a ratio (see SM Table SI [47]). The RPA slightly overestimates these parameters as well as the equilibrium volume. Correspondingly, the energy gain following the AFD rotations and lattice elongation is slightly too large, resulting in a higher T_c. This is related to the reduced accuracy of the RPA in the description of short-range interactions involved in covalent bonds [75,76], such as the Sr-O bond that is mainly responsible for the AFD instability [26]. Note that for all levels of theory, the effect of anharmonicity is to *decrease* the equilibrium value of c/a and the AFD rotation in the tetragonal phase (see SM Table SI [47]). Thus, anharmonicity partly cures the so-called super-tetragonality problem in describing the structural properties.

Moving to the FE instability, we have already shown that anharmonic quantum fluctuations suppress it down to 0 K. We remark that this result does not adopt any model assumptions nor does it suffer from the limitations of path-integral based methods at very low temperatures, where these methods become almost inapplicable [34]. This is precisely the temperature range where the onset of quantum critical effects is observed. However, the question remains of how well the FE soft mode is described by first-principles calculations as compared to the experimental measurements. From Fig. 3(b), we see that both PBEsol and, surprisingly, rSCAN fail to reproduce the very soft experimental frequencies and their temperature dependence. The RPA comes very close to experiment, reproducing the plateau below around 25 K as well as the subsequent increase with temperature. Correspondingly, in SM Fig. S11 [47], we also show that the calculations display the quantum critical scaling of the dielectric function observed experimentally. The energy splitting of the E_u and A_{2u} FE modes is also correctly captured, as shown in Fig. 3(d). The sign and value of the splitting are dictated by the anharmonic relaxation of the c/a ratio (see SM Fig. S10(d) and the related discussion [47]). This effect is not generally taken into account, however, it is tightly linked to the strain-induced ferroelectricity and the onset of quantum criticality.

Since the FE instability is highly sensitive to the lattice volume and shape, as seen in Figs. 1(c)–1(f), we consider the effect of anharmonic lattice expansion using rSCAN. After including this effect, the FE mode frequencies decrease only by about 2 meV as shown in SM Fig. S10(b) [47], hence the experimental values are still largely overestimated. Additional calculations using the hybrid functional HSE06 also yield too hard FE anharmonic peaks (8 meV at 0 K). This confirms that the FE instability and its associated well depth, shown in Figs. 1(a) and 1(b), can only be described accurately using the RPA, which gives a better description of the Ti-O interactions mainly responsible for the FE instability [38]. We argue that this conclusion is rather general and applies to other prototypical ABO_3 perovskites such as $KTaO_3$ and $BaTiO_3$. In the case of $KTaO_3$, anharmonic calculations using SCAN qualitatively reproduced the quantum paraelectric behavior but also yielded too large FE frequencies [77]. Based on our results for $SrTiO_3$ and the calculated FE well depths shown in Fig. 1(g) for $KTaO_3$, we expect that the RPA would again produce softer frequencies in line with experiments. In contrast, HSE06 would predict even larger FE frequencies. $BaTiO_3$ undergoes a transition from a paraelectric cubic phase to a ferroelectric tetragonal one near 400 K. The transition temperature predicted from DFT is too low [35,78], implying that the energy barrier for the transition is underestimated.

Our calculations for $BaTiO_3$ indicate that the increased well depths in the RPA should restore agreement with experiment (see Fig. 1(h) and SM Fig. S12 [47]).

In conclusion, we use machine-learned force fields to perform nonperturbative anharmonic calculations to investigate the quantum paraelectric state in $SrTiO_3$ as well as its AFD transformation between a cubic and tetragonal structure. Our calculations are free from commonly used approximations and are able to accurately characterize the temperature-dependent soft phonon modes. By leveraging Δ-machine learning, we perform RPA-level calculations and show that the RPA predicts soft FE modes in good agreement with the experiment, whereas the most accurate semilocal functionals available do not. We also find that the RPA overestimates the AFD transition temperature, indicating that even beyond-RPA schemes are needed to cure the tendency of the RPA to underbind and overestimate bond lengths and volumes [75,76]. More generally, our work challenges the ability of DFT-based methods to describe key phenomena in quantum paraelectrics and conventional ferroelectrics, namely, dilute superconductivity and quantum criticality [27,79], nonlinear phononics processes [80,81], and electron-phonon coupling effects [82,83]. The approach we demonstrated is general and opens up possibilities to investigate materials exhibiting strong anharmonicity in combination with other unconventional quantum mechanical properties, such as many perovskite structures, lead and tin chalcogenides, and half-Heusler compounds.

C.V. and G.K. gratefully acknowledge many discussions with R. Jinnouchi, F. Karsai and P. Liu. L.R. and C.F. thank L. Monacelli and M. Calandra for helpful suggestions. The computational results have been mainly achieved using the Vienna Scientific Cluster (VSC). This work was supported by the Austrian Science Fund (FWF) within project SFB TACO (Project No. F 81-N).

[1] J. F. Schooley, W. R. Hosler, and M. L. Cohen, Phys. Rev. Lett. **12**, 474 (1964).
[2] N. A. Babushkina, L. M. Belova, O. Y. Gorbenko, A. R. Kaul, A. A. Bosak, V. I. Ozhogin, and K. I. Kugel, Nature (London) **391**, 159 (1998).
[3] R. Guo, L. E. Cross, S.-E. Park, B. Noheda, D. E. Cox, and G. Shirane, Phys. Rev. Lett. **84**, 5423 (2000).
[4] H. Ohta, S. Kin, Y. Mune, T. Mizoguchi, K. Nomura, S. Ohta, T. Nomura, Y. Nakanishi, Y. Ikuhara, M. Hirano, H. Hosono, and K. Koumoto, Nat. Mater. **6**, 129 (2007).
[5] V. Garcia, S. Fusil, K. Bouzehouane, S. Enouz-Vedrenne, N. D. Mathur, A. Barthélémy, and M. Bibes, Nature (London) **460**, 81 (2009).
[6] J. Hwang, R. R. Rao, L. Giordano, Y. Katayama, Y. Yu, and Y. Shao-Horn, Science **358**, 751 (2017).
[7] N. A. Spaldin and R. Ramesh, Nat. Mater. **18**, 203 (2019).
[8] W. Zhong and D. Vanderbilt, Phys. Rev. Lett. **74**, 2587 (1995).
[9] N. A. Benedek and C. J. Fennie, J. Phys. Chem. C **117**, 13339 (2013).
[10] N. Reyren, S. Thiel, A. D. Caviglia, L. Fitting Kourkoutis, G. Hammerl, C. Richter, C. W. Schneider, T. Kopp, A.-S. Rüetschi, D. Jaccard, M. Gabay, D. A. Muller, J.-M. Triscone, and J. Mannhart, Science **317**, 1196 (2007).
[11] A. F. Santander-Syro, O. Copie, T. Kondo, F. Fortuna, S. Pailhes, R. Weht, X. G. Qiu, F. Bertran, A. Nicolaou, A. Taleb-Ibrahimi, P. Le Fevre, G. Herranz, M. Bibes, N. Reyren, Y. Apertet, P. Lecoeur, A. Barthelemy, and M. J. Rozenberg, Nature (London) **469**, 189 (2011).
[12] C. Chen, J. Avila, E. Frantzeskakis, A. Levy, and M. C. Asensio, Nat. Commun. **6**, 8585 (2015).
[13] C. Collignon, X. Lin, C. W. Rischau, B. Fauqué, and K. Behnia, Annu. Rev. Condens. Matter Phys. **10**, 25 (2019).
[14] G. Shirane and Y. Yamada, Phys. Rev. **177**, 858 (1969).
[15] K. A. Müller and H. Burkard, Phys. Rev. B **19**, 3593 (1979).
[16] J. H. Haeni, P. Irvin, W. Chang, R. Uecker, P. Reiche, Y. L. Li, S. Choudhury, W. Tian, M. E. Hawley, B. Craigo, A. K. Tagantsev, X. Q. Pan, S. K. Streiffer, L. Q. Chen, S. W. Kirchoefer, J. Levy, and D. G. Schlom, Nature (London) **430**, 758 (2004).
[17] M. Itoh, R. Wang, Y. Inaguma, T. Yamaguchi, Y.-J. Shan, and T. Nakamura, Phys. Rev. Lett. **82**, 3540 (1999).
[18] S. E. Rowley, L. J. Spalek, R. P. Smith, M. P. M. Dean, M. Itoh, J. F. Scott, G. G. Lonzarich, and S. S. Saxena, Nat. Phys. **10**, 367 (2014).
[19] C. W. Rischau, X. Lin, C. P. Grams, D. Finck, S. Harms, J. Engelmayer, T. Lorenz, Y. Gallais, B. Fauqué, J. Hemberger, and K. Behnia, Nat. Phys. **13**, 643 (2017).
[20] A. Kumar, V. I. Yudson, and D. L. Maslov, Phys. Rev. Lett. **126**, 076601 (2021).
[21] M. N. Gastiasoro, J. Ruhman, and R. M. Fernandes, Ann. Phys. **417**, 168107 (2020).
[22] D. E. Kiselov and M. V. Feigel'man, Phys. Rev. B **104**, L220506 (2021).
[23] P. Chandra, G. G. Lonzarich, S. E. Rowley, and J. F. Scott, Rep. Prog. Phys. **80**, 112502 (2017).
[24] Y.-Y. Pai, A. Tylan-Tyler, P. Irvin, and J. Levy, Rep. Prog. Phys. **81**, 036503 (2018).
[25] N. Sai and D. Vanderbilt, Phys. Rev. B **62**, 13942 (2000).
[26] U. Aschauer and N. A. Spaldin, J. Phys.: Condens. Matter **26**, 122203 (2014).
[27] J. M. Edge, Y. Kedem, U. Aschauer, N. A. Spaldin, and A. V. Balatsky, Phys. Rev. Lett. **115**, 247002 (2015).
[28] P. Souvatzis, O. Eriksson, M. I. Katsnelson, and S. P. Rudin, Comput. Mater. Sci. **44**, 888 (2009).
[29] O. Hellman, I. A. Abrikosov, and S. I. Simak, Phys. Rev. B **84**, 180301(R) (2011).
[30] I. Errea, M. Calandra, and F. Mauri, Phys. Rev. Lett. **111**, 177002 (2013).
[31] T. Tadano and S. Tsuneyuki, Phys. Rev. B **92**, 054301 (2015).
[32] A. van Roekeghem, J. Carrete, and N. Mingo, Comput. Phys. Commun. **263**, 107945 (2021).
[33] M. Zacharias, G. Volonakis, F. Giustino, and J. Even, arXiv:2212.10633.
[34] W. Zhong and D. Vanderbilt, Phys. Rev. B **53**, 5047 (1996).

[35] J. Íñiguez and D. Vanderbilt, Phys. Rev. Lett. **89**, 115503 (2002).

[36] D. Shin, S. Latini, C. Schäfer, S. A. Sato, U. De Giovannini, H. Hübener, and A. Rubio, Phys. Rev. B **104**, L060103 (2021).

[37] T. Esswein and N. A. Spaldin, Phys. Rev. Res. **4**, 033020 (2022).

[38] R. Wahl, D. Vogtenhuber, and G. Kresse, Phys. Rev. B **78**, 104116 (2008).

[39] L. Monacelli, R. Bianco, M. Cherubini, M. Calandra, I. Errea, and F. Mauri, J. Phys.: Condens. Matter **33**, 363001 (2021).

[40] P. Friederich, F. Häse, J. Proppe, and A. Aspuru-Guzik, Nat. Mater. **20**, 750 (2021).

[41] X. Ren, P. Rinke, C. Joas, and M. Scheffler, J. Mater. Sci. **47**, 7447 (2012).

[42] R. Ramakrishnan, P. O. Dral, M. Rupp, and O. A. von Lilienfeld, J. Chem. Theory Comput. **11**, 2087 (2015).

[43] D. J. Hooton, Philos. Mag. J. Sci. **46**, 422 (1955).

[44] T. R. Koehler, Phys. Rev. Lett. **17**, 89 (1966).

[45] U. Aseginolaza, R. Bianco, L. Monacelli, L. Paulatto, M. Calandra, F. Mauri, A. Bergara, and I. Errea, Phys. Rev. Lett. **122**, 075901 (2019).

[46] L. Monacelli, R. Bianco, M. Cherubini, M. Calandra, I. Errea, and F. Mauri, Nat. Phys. **17**, 63 (2021).

[47] See Supplemental Material at http://link.aps.org/supplemental/10.1103/PhysRevMaterials.7.L030801 for details of the first-principles calculations, the MLFF training and validation, the SSCHA method and calculations, and Figs. S1–S12, which includes Refs. [48–55].

[48] M. Kaltak, J. Klimeš, and G. Kresse, Phys. Rev. B **90**, 054115 (2014).

[49] J. Harl, L. Schimka, and G. Kresse, Phys. Rev. B **81**, 115126 (2010).

[50] R. Jinnouchi, F. Karsai, C. Verdi, R. Asahi, and G. Kresse, J. Chem. Phys. **152**, 234102 (2020).

[51] A. P. Bartók, M. C. Payne, R. Kondor, and G. Csányi, Phys. Rev. Lett. **104**, 136403 (2010).

[52] A. Tröster, C. Verdi, C. Dellago, I. Rychetsky, G. Kresse, and W. Schranz, Phys. Rev. Mater. **6**, 094408 (2022).

[53] R. Bianco, I. Errea, L. Paulatto, M. Calandra, and F. Mauri, Phys. Rev. B **96**, 014111 (2017).

[54] L. Cao, E. Sozontov, and J. Zegenhagen, Phys. Status Solidi (a) **181**, 387 (2000).

[55] A. Okazaki and M. Kawaminami, Mater. Res. Bull. **8**, 545 (1973).

[56] V. L. Deringer, M. A. Caro, and G. Csányi, Adv. Mater. **31**, 1902765 (2019).

[57] V. V. Ladygin, P. Y. Korotaev, A. V. Yanilkin, and A. V. Shapeev, Comput. Mater. Sci. **172**, 109333 (2020).

[58] C. Verdi, F. Karsai, P. Liu, R. Jinnouchi, and G. Kresse, npj Comput. Mater. **7**, 156 (2021).

[59] S. Tinte, J. Íñiguez, K. M. Rabe, and D. Vanderbilt, Phys. Rev. B **67**, 064106 (2003).

[60] C. Escorihuela-Sayalero, J. C. Wojdeł, and J. Íñiguez, Phys. Rev. B **95**, 094115 (2017).

[61] R. B. Wexler, Y. Qi, and A. M. Rappe, Phys. Rev. B **100**, 174109 (2019).

[62] J. P. Perdew, A. Ruzsinszky, G. I. Csonka, O. A. Vydrov, G. E. Scuseria, L. A. Constantin, X. Zhou, and K. Burke, Phys. Rev. Lett. **100**, 136406 (2008).

[63] G. Kresse and J. Hafner, Phys. Rev. B **47**, 558 (1993).

[64] G. Kresse and J. Furthmüller, Phys. Rev. B **54**, 11169 (1996).

[65] R. Jinnouchi, F. Karsai, and G. Kresse, Phys. Rev. B **100**, 014105 (2019).

[66] A. P. Bartók and J. R. Yates, J. Chem. Phys. **150**, 161101 (2019).

[67] J. Heyd, G. E. Scuseria, and M. Ernzerhof, J. Chem. Phys. **118**, 8207 (2003).

[68] A. V. Krukau, O. A. Vydrov, A. F. Izmaylov, and G. E. Scuseria, J. Chem. Phys. **125**, 224106 (2006).

[69] L. Schimka, J. Harl, A. Stroppa, A. Grüneis, M. Marsman, F. Mittendorfer, and G. Kresse, Nat. Mater. **9**, 741 (2010).

[70] B. Ramberger, T. Schäfer, and G. Kresse, Phys. Rev. Lett. **118**, 106403 (2017).

[71] P. Liu, C. Verdi, F. Karsai, and G. Kresse, Phys. Rev. B **105**, L060102 (2022).

[72] R. Cowley, W. J. L. Buyers, and G. Dolling, Solid State Commun. **7**, 181 (1969).

[73] A. Yamanaka, M. Kataoka, Y. Inaba, K. Inoue, B. Hehlen, and E. Courtens, Europhys. Lett. **50**, 688 (2000).

[74] Y. Yamada and G. Shirane, J. Phys. Soc. Jpn. **26**, 396 (1969).

[75] J. Paier, X. Ren, P. Rinke, G. E. Scuseria, A. Grüneis, G. Kresse, and M. Scheffler, New J. Phys. **14**, 043002 (2012).

[76] S. Ruan, X. Ren, T. Gould, and A. Ruzsinszky, J. Chem. Theory Comput. **17**, 2107 (2021).

[77] L. Ranalli, C. Verdi, L. Monacelli, G. Kresse, M. Calandra, and C. Franchini, Adv. Quantum Technol. 2200131 (2023).

[78] L. Gigli, M. Veit, M. Kotiuga, G. Pizzi, N. Marzari, and M. Ceriotti, npj Comput. Mater. **8**, 209 (2022).

[79] P. A. Volkov, P. Chandra, and P. Coleman, Nat. Commun. **13**, 4599 (2022).

[80] X. Li, T. Qiu, J. Zhang, E. Baldini, J. Lu, A. M. Rappe, and K. A. Nelson, Science **364**, 1079 (2019).

[81] M. Kozina, M. Fechner, P. Marsik, T. van Driel, J. M. Glownia, C. Bernhard, M. Radovic, D. Zhu, S. Bonetti, U. Staub, and M. C. Hoffmann, Nat. Phys. **15**, 387 (2019).

[82] J.-J. Zhou, O. Hellman, and M. Bernardi, Phys. Rev. Lett. **121**, 226603 (2018).

[83] M. Zacharias, M. Scheffler, and C. Carbogno, Phys. Rev. B **102**, 045126 (2020).